Nanoporous PtFe alloys as highly active and durable electrocatalysts for oxygen reduction reaction

CrossMark

Huimei Duan, Qin Hao, Caixia Xu[*]

Key Laboratory of Chemical Sensing & Analysis in Universities of Shandong, School of Chemistry and Chemical Engineering, University of Jinan, Jinan 250022, China

HIGHLIGHTS

- NP–PtFe alloys with different ratios were made via two-step dealloying method.
- NP–PtFe alloys show higher mass and specific ORR activities than PtFe/C and Pt/C.
- NP–PtFe alloys exhibit much higher structure stability than PtFe/C and Pt/C.
- The ORR performance follows the order of NP–$Pt_{75}Fe_{25}$ > NP–$Pt_{55}Fe_{45}$ > PtFe/C > Pt/C.

GRAPHICAL ABSTRACT
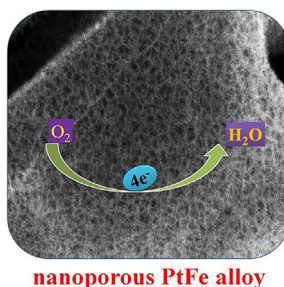
nanoporous PtFe alloy

ABSTRACT

Nanoporous PtFe alloys with two different bimetallic ratios are fabricated by selectively dealloying PtFeAl ternary alloys, characterized by nanoscaled bicontinuous network skeleton with interconnected hollow channels extending in all three dimensions. The reactive components in PtFeAl ternary alloy were sequentially leached out in a highly controllable manner, generating nanoporous architecture with different bimetallic ratios and the typical ligament size as small as 5 nm. These nanoporous PtFe alloys exhibit much enhanced electrocatalytic activity for oxygen reduction reaction compared with the PtFe/C and Pt/C catalysts. The specific and mass activities for oxygen reduction follow the order of nanoporous $Pt_{75}Fe_{25}$ > nanoporous $Pt_{55}Fe_{45}$ > PtFe/C > Pt/C. In the absence of any catalyst support, the structure stability of nanoporous PtFe alloys is greatly enhanced with less loss of the electrochemical surface area and the oxygen reduction activity upon long-term potential scan tests compared with PtFe/C and Pt/C catalysts. The as-made nanoporous PtFe alloys thus hold great application potential as promising cathode electrocatalyst in proton exchange membrane fuel cells with the advantages of easy preparation along with superior oxygen reduction activity and durability.

© 2014 Elsevier B.V. All rights reserved.

1. Introduction

Proton exchange membrane fuel cells (PEMFCs) have attracted considerable attention because of their great application potential as alternative energy sources in the fields of automobile transportation and portable electronics [1–4]. Oxygen reduction reaction (ORR), the main reaction that takes place at the fuel cell cathode, is vital for various PEMFCs to achieve the desirable energy output efficiency and utilization lifetime [5–8]. It is well-known that Pt represents an important class of metallic cathode catalysts in terms of their high catalytic activity toward ORR [9–12]. Although considerable research has been focused on improving the performance of non-Pt catalysts, Pt-based catalysts still represent the highest ORR activity [13–15]. At present, the popular

* Corresponding author.
  E-mail addresses: chm_xucx@ujn.edu.cn, chemxucx@gmail.com (C. Xu).

commercial ORR catalyst is in a form of fine Pt nanoparticles (~3 nm) dispersed on carbon supports [3]. However, a series of problems, such as corrosion of the carbon support, de-adhesion between the catalyst and support, and the dissolution/aggregation/Ostwald ripening of Pt nanoparticles, usually induce large loss of the electrochemical surface area (ECSA) and ORR activity degradation during long-term operation [16–21].

In order to promote the practical applications of Pt, it is essential to pay more attention to the design and engineering of highly active Pt-based nanocatalysts for ORR by alloying with other transition metals and/or modifying the morphology [22]. Recently, non-precious Fe, as one of the 3d transition metals, has been found to have great synergistic catalytic effect on the ORR activity of Pt in terms of enhanced activity and reduced Pt loadings [8,23]. For instance, Toda et al. [24] found that supportless Pt–Fe bulk alloys showed improved ORR activity compared with pure Pt. Malheiro et al. [25] fabricated Pt–Fe/C alloy catalysts through a polyol process by using hexadecanediol as reducing agent, and oleic acid and oleylamine as stabilizers, finding an improved ORR activity compared to Pt/C catalyst. Despite lots of reports about the ORR activities on Pt–Fe alloy nanomaterials, the effects of the bimetallic ratio on the ORR activities, the structure stability, and the activity origination are much less investigated.

In order to maximize the ORR activities of PtFe alloys, it is necessary to optimize the morphology of the catalysts as well as the alloy compositions. Thus, it is desired to fabricate highly active nanocatalysts with high intrinsic catalytic activity and durability. Recently, nanoporous metallic materials made by dealloying method have received great attention because a unique combination of a highly conductive network and a highly accessible open nanoporosity is favorable for the electron and mass transportation during electrocatalysis [26–30]. In addition, nanoporous metallic materials can be easily fabricated by dealloying from a binary or multi-component alloy [31–34]. In this paper, we reported the nanoporous (NP) PtFe alloy electrocatalysts fabricated through a two-step dealloying process by sequentially leaching out the reactive components from PtFeAl ternary alloy. NP–PtFe alloys show distinct ORR performance with the alteration of Fe content. Meanwhile, we investigated the effects of bimetallic ratios in NP–PtFe alloys on the ORR activities and structure stability, and further explored the activity origination by density functional theory calculations.

2. Experimental section

$Pt_{11}Fe_9Al_{80}$ (at.%) ternary alloy foils were prepared by refining the corresponding metals Pt, Fe, and Al (99.99%) in an arc-furnace, followed by melt-spinning under an Ar-protected atmosphere [35]. All agents were obtained from Shanghai Sinopharm Chemical Reagent Ltd. Co of China and used as an analytic purity. In a typical experiment, nanoporous PtFe (NP–$Pt_{55}Fe_{45}$) alloys were first fabricated by dealloying PtFeAl alloy foils in 0.5 M NaOH solution at room temperature for 48 h. The NP–$Pt_{55}Fe_{45}$ alloys were further treated in dilute HNO_3 (1.5 M) at room temperature for 5 h to prepare NP–$Pt_{75}Fe_{25}$ alloy. The products were washed for several times with ultra-pure water (18.2 MΩ) and dried at room temperature in air. During the preparation of carbon-supported PtFe/C nanoparticles, Vulcan XC-72 carbon black was pretreated in 6 M HNO_3 solution at 100 °C for 4 h [36] and a feeding mole ratio between platinum and iron is controlled at 75:25. The other procedure was operated completely according to the work by Xu et al. [37]. The John-Matthey Pt/C (20 wt.% on carbon) catalysts were purchased from Alfa Aesar.

Powder X-ray diffraction (XRD) data were collected on a Bruker D8 advanced X-ray diffractometer using Cu Kα radiation

($\lambda = 1.5418$ Å) at a scan rate of 0.04° s^{-1}. The structure and chemical composition of all samples were characterized on a JEOL JSM-6700F field emission scanning electron microscope (SEM), equipped with an Oxford INCA X-sight energy dispersive X-ray spectrometer. Transmission electron microscopy (TEM) images were obtained with a JEM-2100 high-resolution transmission electron microscope (200 kV).

All electrochemical measurements were performed on a PINE AFCBP1 electrochemical workstation using a conventional three electrode cell with Pt foil as a counter electrode and mercury sulfate electrode as the reference electrode. The ORR activity was measured on MSR rotation ring-disk electrode (RDE, Phychemi Company Limited) in an O_2-saturated 0.1 M $HClO_4$ solution. All potentials in the current manuscript are provided with respect to the reversible hydrogen electrode. All NP–PtFe catalyst suspensions were prepared by sonicating 1.8 mg of catalyst sample, 1.5 mg of carbon powder, 400 μL of ethanol, and 200 μL of Nafion solution (0.5 wt.%) for one hour. Pt/C catalyst ink (about 1 mg mL^{-1}) was also prepared in a similar way except the further addition of carbon powder. Appropriate catalyst inks were dropped onto a pre-polished rotating disk electrode (5 mm in diameter) and dried for following measurement. The loadings of Pt for Pt/C, PtFe/C, NP–$Pt_{55}Fe_{45}$, and NP–$Pt_{75}Fe_{25}$ catalysts were determined to be 15.7, 14.2, 17.5, and 14.0 μg cm^{-2}, respectively. Prior to electrochemical measurements, the electrolytes were deoxygenated by bubbling N_2 for 30 min except for the ORR measurements. All ORR experiments were performed in O_2 saturated 0.1 M $HClO_4$ at a scan rate of 10 mV s^{-1}. The ECSAs of the Pt-based electrodes were calculated by integrating the charge associated with H desorption in N_2-purged 0.1 M $HClO_4$ solution at the scan rate of 50 mV s^{-1}, in which the value of the used charge density for the desorption of a hydrogen monolayer is 210 μC cm^{-2} Pt with the double layer corrected. The ECSAs of NP–$Pt_{55}Fe_{45}$, NP–$Pt_{75}Fe_{25}$, PtFe/C, and Pt/C were measured to be 36, 50, 54, and 73 m^2 g^{-1}, respectively.

All density functional theory (DFT) calculations were performed with VASP program [38], using the gradient-corrected PBE exchange-correlation functional [39]. The electronic wave functions were expanded in a plane wave basis set with an energy cutoff of 400 eV. For all the cases, a four-layer slab model with the forth layer fixed was employed. Repeated slabs were separated by more than 10 Å to avoid interaction between each other. The 2 × 2-unit cell $Pt_{56}Fe_{44}$ (111) slabs with pure Pt in the first layer and 75% Pt in the second layer, and 50% Pt in the third and fourth layers were used to model the case of the used catalysts. The 2 × 2-unit cell $Pt_{75}Fe_{25}$ (111) slabs with pure Pt in the first layer and 50% Pt in the second layer, and 25% Pt in the third and fourth layers were used to model the case of the used catalysts. The optimized geometries were obtained when the forces on all the unconstrained atoms were smaller in magnitude than 0.02 eV Å^{-1}. The Brillouin zone integration was done on a grid of 5 × 5 × 1 using the Monkorst–Pack k-points [40]. The density of state calculations were calculated at the same level except with a 13 × 13 × 1 Monkorst–Pack k-points mesh. On all the surfaces considered in this study, oxygen atom adsorbed at fcc hollow site is the most favorable. The oxygen adsorption energy ΔE_O is defined as $\Delta E_O = E(slab) + E(O) - E(ads/M)$ and ΔE_{OH} is defined as $\Delta E_{OH} = E(slab) + E(OH) - E(ads/M)$, where $E(slab)$, $E(O)$, and $E(OH)$ are the energies of the clean slab, and isolate oxygen atom and OH in vacuum, respectively, and $E(ads/M)$ is the energy of the adsorbate-M adsorption system.

3. Results and discussion

To achieve a simple and controllable preparation for nanoporous PtFe alloy, PtFeAl ternary alloy was selected as the source precursor

because Al is more reactive and can be dissolved in a common alkaline solution under free corrosion without any loss of Pt and Fe. Meanwhile, Fe is more reactive compared with Pt, and thus the Fe atoms can be further selectively etched to achieve the desired bimetallic ratio. Energy-dispersive spectroscopy (EDS) was first used to analyze the composition of the PtFeAl source alloy. As shown in Fig. 1(a) the alloy component is $Pt_{11}Fe_9Al_{80}$ (at.%), which is consistent with our initial designed ratio [35]. Fig. 1(b) indicates that the bimetallic ratio between Pt and Fe in the first dealloyed sample is around 55:45, which is consistent with the initial feeding ratio of Pt and Fe. Fig. 1(c) indicates that the bimetallic ratio between Pt and Fe in the resulted sample after further dealloying in 1.5 M HNO_3 solution is around 75:25. EDS analysis demonstrated an excellent control to the resulted alloy composition with successive dealloying treatment. Meanwhile, a most majority of Al atoms were removed upon dealloying. Possibly, the little residual Al atoms are buried within the nanoporous structure, which could not affect the surface reactivity of the as-made catalysts.

The microstructures of the dealloyed samples were characterized by electron microscopes. By one-step selective etching of PtFeAl alloy in 0.5 M NaOH solution, an open nanosponge structure was successfully fabricated as shown in Fig. 2. From the SEM image (Fig. 2(a)), it can be clearly found that the resulted structure upon

dealloying is composed of many interconnected micro-ribbons with the diameter of hundreds of nanometers. It is noted that the resulted structure upon dealloying in 0.5 M NaOH has larger ribbon size and less voids distributed on the surface, which is different with that in 2 M NaOH solution [35]. It is considered that the etching rate in 2 M NaOH is more rapid that in 0.5 M NaOH solution. The rapid etching rate accompanied with the rapid release of hydrogen from the surface led to the larger voids and relatively narrow ribbons. From a high-magnification SEM image (Fig. 2(b)), it is interesting to find that the micro-ribbons also consist of uniform network nanostructure with narrow ligament and pore channel distributions. Meanwhile, cross-section SEM (Fig. 2(c)) further demonstrated that NaOH solution has penetrated the whole sample with uniform porosity extending in all dimensions. Detailed structure was further characterized by TEM. The clear contrast between the interconnected dark skeletons and inner bright regions in TEM image (Fig. 2(d)) provides further evidence for the formation of the nanosponge architecture. From the high-resolution TEM (HRTEM) image (Fig. 2(e)), continuous lattice fringes were resolved across several pores with the lattice space calculated to be ~2.15 Å, corresponding to the (111) plane spacing for PtFe alloy. The typical ligament size for NP–PtFe mainly distributed at ~5 nm based on the HRTEM image. The resulted NP–$Pt_{75}Fe_{25}$ upon partly etching Fe in HNO_3 solution was further examined. Fig. 2(f) shows that the microstructure of the NP–$Pt_{75}Fe_{25}$ alloy is similar to that of NP–$Pt_{55}Fe_{45}$ alloy with uniform network nanostructure with narrow ligament and pore channel distributions. A typical TEM image is displayed as Fig. 2(f) inset, which provides further evidence for the formation of the nanosponge architecture.

To gain insight into the structure formation, XRD was used to examine the crystal structure of PtFe samples. In comparison to the diffraction pattern of the PtFeAl source alloy (Fig. 3) [35], the two NP–PtFe samples show a set of three broad diffraction peaks, which is similar to those of pure Pt. The NP–$Pt_{75}Fe_{25}$ sample shows smaller diffraction angles than that of the NP–$Pt_{55}Fe_{45}$ sample, which reveals the lower Fe content upon further dealloying. These peaks can be assigned to the (111), (200), (220) diffractions for a face centered cubic (fcc) structure, indicating that Fe atoms uniformly distributed into the fcc structure of Pt [41,42]. The broad diffraction feature in the two NP–PtFe alloys are due to the smaller structure dimensions of the NP–PtFe alloy nanostructure as observed in SEM and TEM characterizations. In addition, there are some weak diffractions (marked with an asterisk) existed, which can be indexed to the Fe_3O_4 species. The formation of Fe oxides can be attributed to the oxidation of Fe atoms on the NP surface during the drying procedure. Different concentration of NaOH solution can account for the formation of Fe_3O_4 species instead of Fe_2O_3 species as observed in our previous work [35]. Despite the formation of different kinds of Fe oxides, the formation of open interconnected network nanoporous architecture was not influenced, meanwhile which will be dissolved in the potential scan in the acid solution as discussed below.

In previous reports, nanoporous metallic materials prepared by dealloying method have been demonstrated to be an ideal class of ORR electrocatalysts [43–45], in which the microscopic nanoscaled bicontinuous architecture favors the electron conductivity and the enhancement of structure stability. Meanwhile, the interconnected hollow void running through the network skeleton is beneficial for the molecule transport along the channels. Such the integral architecture is the desired multifunctional electrocatalyst structure. Consequently, we focus on the ORR performance of two different NP–PtFe catalysts with a view to exploring their potential applications as highly active Pt-based cathode catalysts. Fig. 4(a) presents the voltammetric behavior of NP–$Pt_{75}Fe_{25}$ sample as the
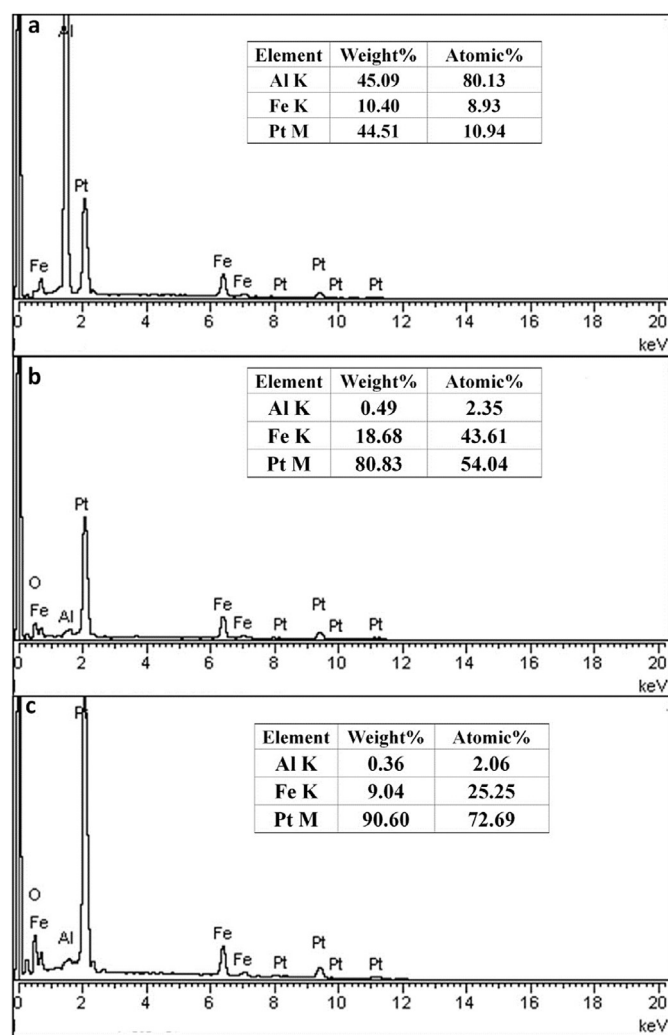

Element	Weight%	Atomic%
Al K	45.09	80.13
Fe K	10.40	8.93
Pt M	44.51	10.94

Element	Weight%	Atomic%
Al K	0.49	2.35
Fe K	18.68	43.61
Pt M	80.83	54.04

Element	Weight%	Atomic%
Al K	0.36	2.06
Fe K	9.04	25.25
Pt M	90.60	72.69

Fig. 1. EDS spectra of the (a) PtFeAl alloy, (b) the first dealloyed sample (NP–$Pt_{55}Fe_{45}$) in 0.5 M NaOH solution at room temperature for 48 h, and (c) the resulted sample (NP–$Pt_{75}Fe_{25}$) after further dealloying in 1.5 M HNO_3 at room temperature for 5 h.
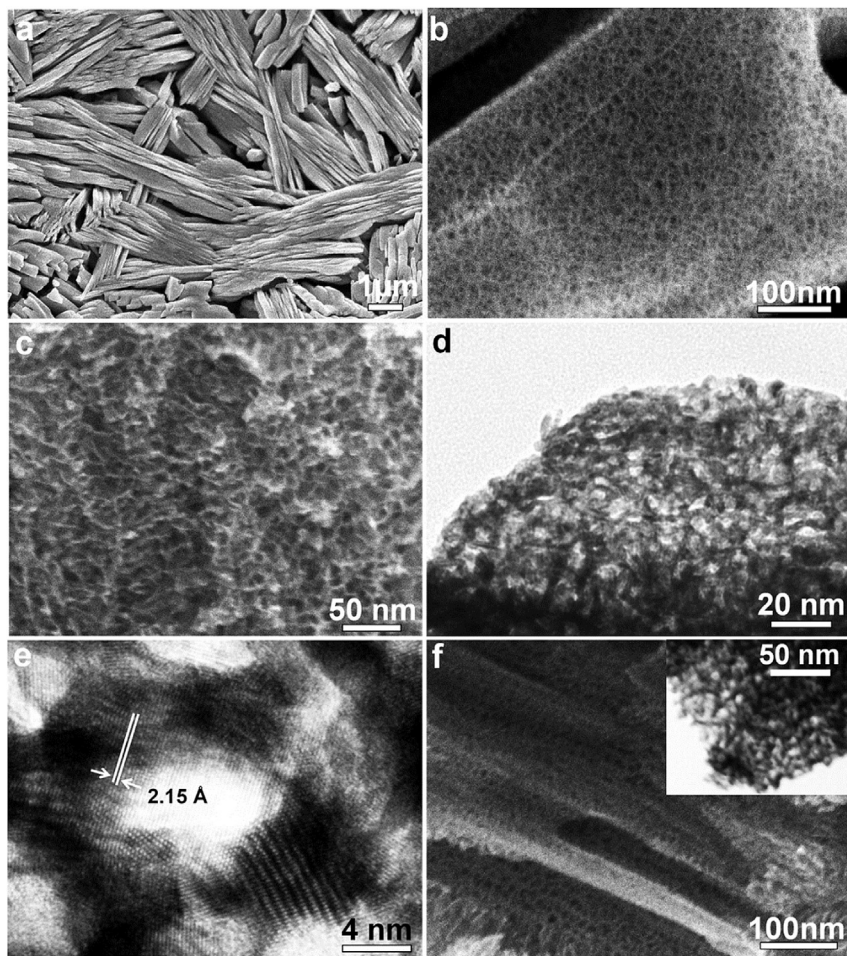
Fig. 2. SEM (a, b), cross-section SEM (c), TEM (d), and HRTEM (e) images of the resulted sample by dealloying of PtFeAl alloy in 0.5 M NaOH solution for 48 h at room temperature and SEM (f) images of further dealloying of NP−Pt$_{55}$Fe$_{45}$ alloy in 1.5 M HNO$_3$ solution for 5 h at room temperature. Inset of (f) is the corresponding TEM image of NP−Pt$_{75}$Fe$_{25}$.

representative. During the first scan, the anodic peak at 0.62–0.86 V originated from the leaching of exposed Fe atoms from the PtFe alloy and Fe oxides on the surface layer. In the subsequent scans, the dissolution peak gradually weakened and negatively shifts. With the continuous CV scan, the hydrogen region (0–0.4 V) gradually evolves into a well-defined voltammetric profile of hydrogen absorption/desorption. Meanwhile, the reduction peak for platinum oxide shifts slightly toward the positive potential and eventually stabilizes at ~0.70 V. Upon several tens of cycles, the weak Fe dissolution peak can also be found, indicating slow dissolution of Fe atoms from a nearly pure Pt-skin alloy surface in 0.1 M HClO$_4$ solution. Compared with the continuous potential sweeps in 0.5 M H$_2$SO$_4$ solution [46], relatively dilute electrolyte solution (0.1 M HClO$_4$ solution) can account for the slow disappearance of the Fe dissolution peak accompanied with the increase of scan cycles.

Fig. 4(b) provides the polarization curves of NP−PtFe alloys in 0.1 M oxygen-saturated HClO$_4$ solution at room temperature with the profile of PtFe/C and commercial Pt/C catalysts included. All curves exhibit two distinguishable potential regions, namely a mixed kinetic-diffusion control region between 0.8 and 1.0 V and a well-defined diffusion controlled region below 0.8 V. The specific activity based on kinetic current density normalized by ECSA was also examined for all catalysts. As shown in Fig. 4(c), it is clearly indicated that both NP−Pt$_{55}$Fe$_{45}$ and NP−Pt$_{75}$Fe$_{25}$ alloys have much higher specific kinetic activities than those of PtFe/C and Pt/C

catalysts in the whole potential range (0.85–0.95 V). For instance, the current densities at 0.90 V are about 0.34 and 0.54 mA cm^{-2} (Fig. 4(d)) for NP−Pt$_{55}$Fe$_{45}$ and NP−Pt$_{75}$Fe$_{25}$ alloys, which are 2.3 and 3.6 times of Pt/C catalyst (~0.15 mA cm^{-2}) [47], and also higher
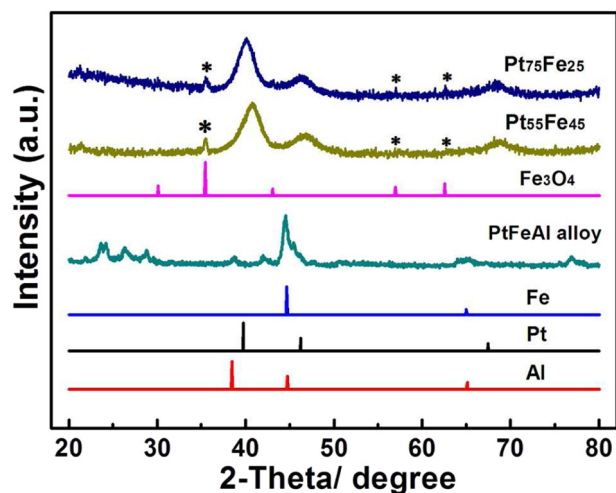

Fig. 3. XRD patterns of the PtFeAl alloy and two de-alloyed samples of different bimetallic ratios. The standard patterns of Pt (JCPDS 65-2868), Al (JCPDS 65-2869), Fe (JCPDS 06-0696), and Fe$_3$O$_4$ (JCPDS 65-3127) are attached for comparison.
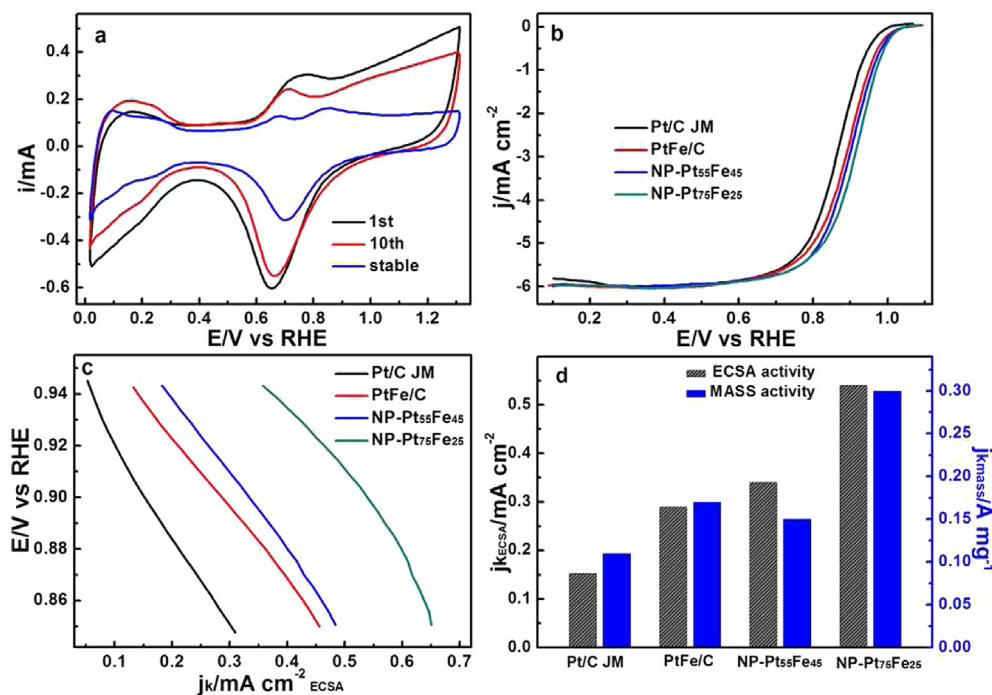
Fig. 4. (a) Cyclic voltammetric curves (CVs) of NP–$Pt_{75}Fe_{25}$ in 0.1 M N_2-purged $HClO_4$ solution. Scan rate: 50 mV s^{-1}, (b) polarization curves for the ORR on NP–$Pt_{75}Fe_{25}$, NP–$Pt_{55}Fe_{45}$, PtFe/C, and Pt/C catalysts in the O_2-saturated 0.1 M $HClO_4$ solution at room temperature at 1600 rpm, Scan rate: 10 mV s^{-1}, (c) specific kinetic current densities for all catalysts at different potentials, (d) specific kinetic and mass kinetic current densities at room temperature for all catalysts at 0.90 V.

than that of PtFe/C (~0.28 mA cm^{-2}). Fig. 4(d) also shows the mass activities of all catalysts at 0.90 V calculated by normalizing the kinetic currents to the Pt loadings. The mass specific activity of NP–$Pt_{75}Fe_{25}$ is nearly 2 times of that of PtFe/C (~0.17 A mg^{-1}), and is about 2.7 times of that of Pt/C catalyst (0.11 A mg^{-1}), while that of NP–$Pt_{55}Fe_{45}$ is very close to that of PtFe/C as well as higher than that of Pt/C catalyst. In this study, the measured activities of the commercial Pt/C catalyst are similar to the reported in other literature [48]. It is clear that NP–$Pt_{75}Fe_{25}$ has superior specific and mass activities among all catalysts. Thus, alloying Pt with appropriate Fe contents not only greatly enhances the specific kinetic activity of Pt catalyst for ORR [42] but also achieves higher mass activity than PtFe/C and Pt/C catalysts.

The catalytic stability for electrocatalysts is significant for their practical application [44,49,50]. It is interesting to explore the structure stability of two different NP–PtFe alloys compared with PtFe/C and Pt/C catalysts. A long-term stability test was carried out by applying continuous potential sweeps in acid solution [13]. With the gradual dissolution of surface Fe atoms from PtFe alloy, a Pt-rich PtFe surface alloy was formed. Meanwhile, the reactivity of Fe atoms was passivated by the ambient Pt atoms. Thus several tens of CV cycles is difficult to eliminate the weak Fe dissolution peak, which further demonstrates the formation of relatively stable nearly Pt-skin PtFe alloy. As shown in Fig. 5(a) and (c), it is obvious that upon 5, 000 cycles the weak Fe dissolution peak completely disappeared with the reduced intensity of Pt reduction peak due to the further dissolution of surface Fe atoms. NP–$Pt_{75}Fe_{25}$ alloy showed almost no degradation with a negative half-wave shift by 1 mV corresponding to almost no loss of the ECSA (Fig. 5(a) and (b)). For the NP–$Pt_{55}Fe_{45}$ catalyst, activity enhancement for ORR activity was observed with a half-wave potential increased by ~10 mV and a decrease of 6% of the ECSA (Fig. 5(c) and (d)). The high catalytic stability of NP–$Pt_{55}Fe_{45}$ can be attributed to the achievement of more favorable PtFe alloy composition with the dissolution of Fe atoms in the surface layers upon long term CV cycles. The ORR

activity of PtFe/C and Pt/C catalyst showed the degradation of ~15 and ~22 mV in half-wave potential during the cycling period with about 12% and 19% loss of ECSA relative to the initial value, respectively (Fig. 5(e) and (f)). By comparison, it is clear that NP–PtFe catalysts show much higher catalytic stability than PtFe/C catalyst and especially higher than Pt/C catalyst despite the combination of more reactive Fe elements, which is obviously related to the specific structure configuration of this catalyst. It is known to us that the lower long-term stability of PtFe/C and Pt/C catalysts results from the corrosion of the carbon support and the dissolution/aggregation/Ostwald ripening of Pt nanoparticles [10]. For NP–PtFe alloy catalysts, an interconnected network skeleton avoids the loss from the corrosion of the carbon support and nanoparticle aggregation.

We further explored the steady-state specific activities of NP–$Pt_{75}Fe_{25}$ and NP–$Pt_{55}Fe_{45}$ alloys by using potentiostatic method along with PtFe/C and Pt/C catalysts. As shown in Fig. 6, at the beginning the potentiostatic currents decreased quickly for all catalysts due to the formation of double layer capacitance. The following current decrease should originate from the loss of surface active sites caused by the adsorption of oxygen-containing intermediate species on the catalyst surface [51,52]. From Fig. 6, the currents for Pt/C and PtFe/C catalysts decreased more rapidly compared with two NP–PtFe alloys at the early reaction stage. With intending the reaction time, all catalysts gradually achieve the relatively stable current. Among all catalysts, NP–$Pt_{75}Fe_{25}$ maintained the highest steady-state current within the whole period of 7200 s with the less loss. Pt/C catalyst underwent the largest current loss, while the PtFe/C catalyst also lost larger than NP–PtFe alloys. By comparison, it is clear that NP–PtFe alloys indicate the superior long-term catalytic durability towards ORR with lower current loss than PtFe/C and Pt/C catalysts.

On the basis of the experimental tests in the present work, we can conclude that incorporation of 25 at.% Fe into Pt is beneficial to maximize the ORR performances of Pt, which is in agreement with
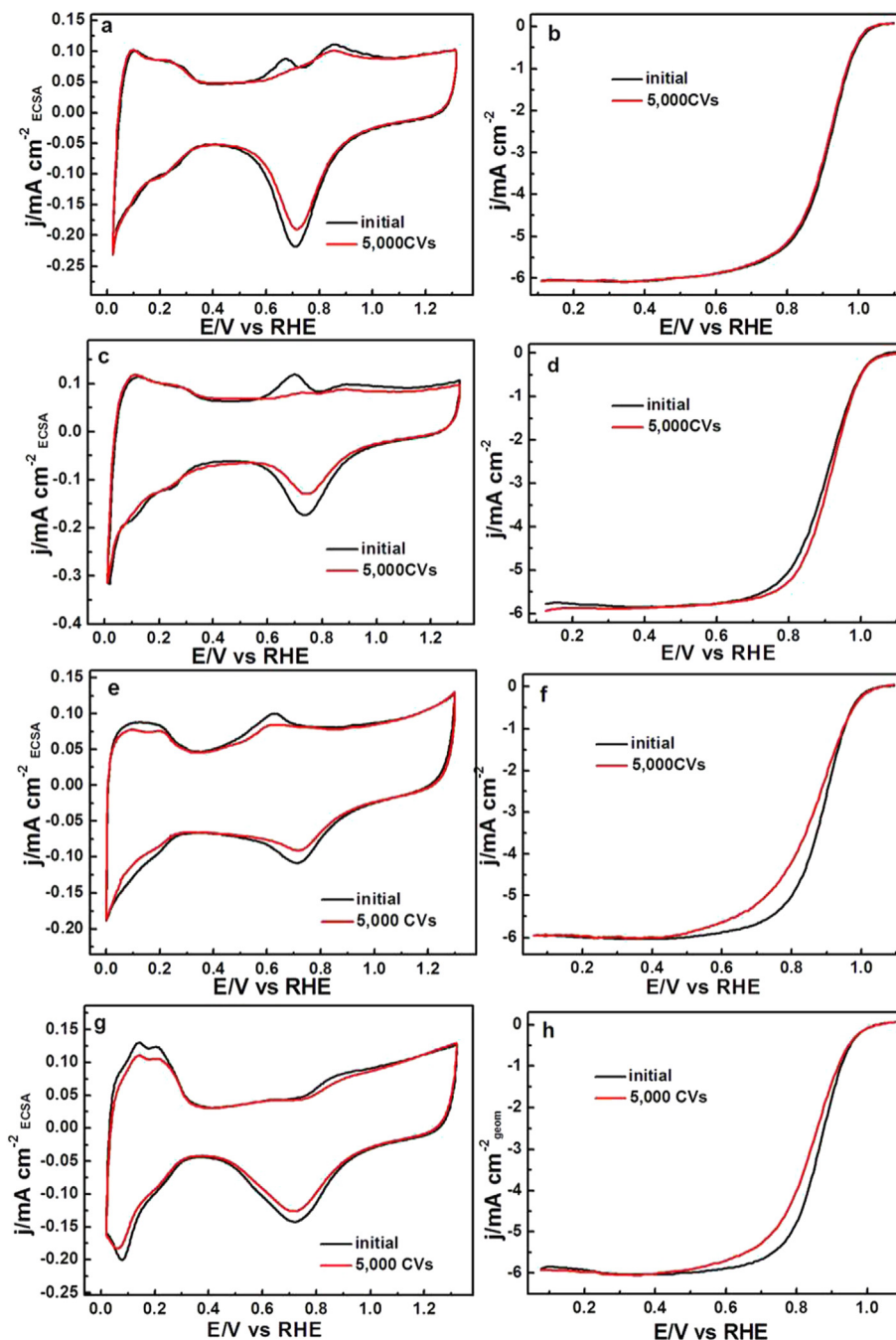
Fig. 5. CVs of NP–Pt$_{75}$Fe$_{25}$ (a), NP–Pt$_{55}$Fe$_{45}$ (c), PtFe/C (e), and Pt/C (g) in 0.1 M HClO$_4$ before and after treated 5000 cycles in 0.1 M HClO$_4$ from 0.6 to 1.0 V vs the reversible hydrogen electrode (RHE). The ORR curves of NP–Pt$_{75}$Fe$_{25}$ (b), NP–Pt$_{55}$Fe$_{45}$ (d), PtFe/C (f), and Pt/C (h) in O$_2$-saturated 0.1 M HClO$_4$ before and after 5000 potential cycles.

previous findings of a maximum activity for catalysts containing 20–30% of Fe [53]. As for the greatly enhanced performance on these NP–PtFe alloys, nanoporous architectures are suggested to play important roles, in which the bicontinuous void space provides the integral molecular transport paths, and the interconnected nanoscaled skeleton allows good electron conductivity as well effectively suppress the structure coarsening. In addition, during the CV scan the surface Fe atoms are progressively dissolved, while the neighboring surface Pt atoms undergo a reconstruction to form a unique alloy structure with a nearly pure Pt-skin [39]. The topmost Pt atoms on the surface may have a compressed strain effect due to the larger difference of lattice parameter between Pt

and Fe, which will decrease the adsorption energy for the reaction intermediates such as O [35,41].

DFT calculations were used to explore the physical origination for the enhanced ORR activity for NP–PtFe alloys. From Fig. 7, the d-band center of Pt in Pt$_{75}$Fe$_{25}$ modal alloy located at −2.86 eV. A negative shift occurs compared with that of pure Pt (−2.72 eV). With the increase of Fe content the Pt d band center in Pt$_{56}$Fe$_{44}$ negatively shifted to −2.96 eV. It is clear that the d band centers of Pt both shift negatively over two PtFe alloys with different compositions, which is in agreement with the XPS observation in previous reports [24,35]. From the change of d band center of Pt, it is difficult to explain the activity difference of NP–PtFe alloys with
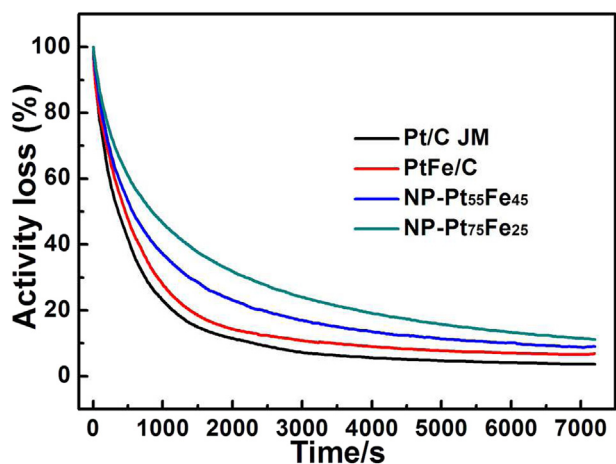
Fig. 6. The corresponding relative loss of electrochemical potentiostatic currents for NP−Pt$_{75}$Fe$_{25}$, NP−Pt$_{55}$Fe$_{45}$, PtFe/C and Pt/C in an oxygen-saturated 0.1 M HClO$_4$ solution at 1600 rpm at 0.90 V vs RHE.

[41,54,55], which is considered to be the intrinsic origination for the higher ORR activity of NP−PtFe alloys than Pt/C. In the numerous studies on the ORR activity over Pt-based alloy, alloying Pt with other transition metals is usually employed to decrease the ΔE_O on pure Pt in order to further enhance its ORR activity [56,57]. OH adsorption energy (ΔE_{OH}) on Pt$_{75}$Fe$_{25}$ (111) slabs was calculated to be −6.87 eV on the most stable bridge sites, which also decreased in comparison to the −6.96 eV on pure Pt(111). With the increase of Fe content the ΔE_{OH} on Pt$_{56}$Fe$_{44}$ is calculated to be −8.39 eV, corresponding to the most stable bridge sites, which is markedly higher than that on Pt(111) and Pt$_{75}$Fe$_{25}$(111) slabs. OH$_{ads}$ generated on the catalyst surface during ORR are poisoning, which usually occupy the surface active sites and block the adsorption of O$_2$. This can account for the relatively lower ORR activity and catalytic durability of NP−Pt$_{55}$Fe$_{45}$ than NP−Pt$_{75}$Fe$_{25}$ despite the reduced ΔE_O. On the basis of these results, it can be concluded that the OH adsorption also play important roles in the oxygen reduction reaction besides the reduced ΔE_O and the more negative d band center of Pt. It is concluded that the incorporation of appropriate Fe content in Pt alloy can greatly enhance its ORR activity by properly tuning the electron structure of Pt [42].

different compositions towards ORR. The adsorption of O and OH on PtFe alloys and pure Pt were further explored by DFT calculations. The oxygen adsorption energies ΔE_O on Pt$_{75}$Fe$_{25}$ (111) slab was calculated to be −3.92 eV with the most stable hcp site (Fig. 7). It is also of interest to find that ΔE_O on Pt$_{56}$Fe$_{44}$ (111) slab continuously decreased to −3.48 eV with the further negative shift of Pt d band center. By comparison, the ΔE_O on PtFe alloy is much lower than that on Pt (111) slab (−4.24 eV). It is proposed that the downshift of d-band center relative to the Fermi level will lead to a downshift of the antibonding states between the oxygen 2p states and the metal d states, generating a weaker metal−O bond

4. Conclusions

Nanoporous PtFe alloys with uniform ligament size and controllable bimetallic ratio are easily fabricated by a mild dealloying process, which show enhanced specific and mass activity for ORR and structure stability compared with PtFe/C and Pt/C. Especially, NP−Pt$_{75}$Fe$_{25}$ shows superior ORR activities compared with NP−Pt$_{55}$Fe$_{45}$, PtFe/C, and Pt/C due to the lower O and OH adsorption energy as demonstrated by DFT calculations, indicating that the alloy ratio has a significant effect on the catalytic behavior in view of the appropriate alloying effect besides the unique nanoporous
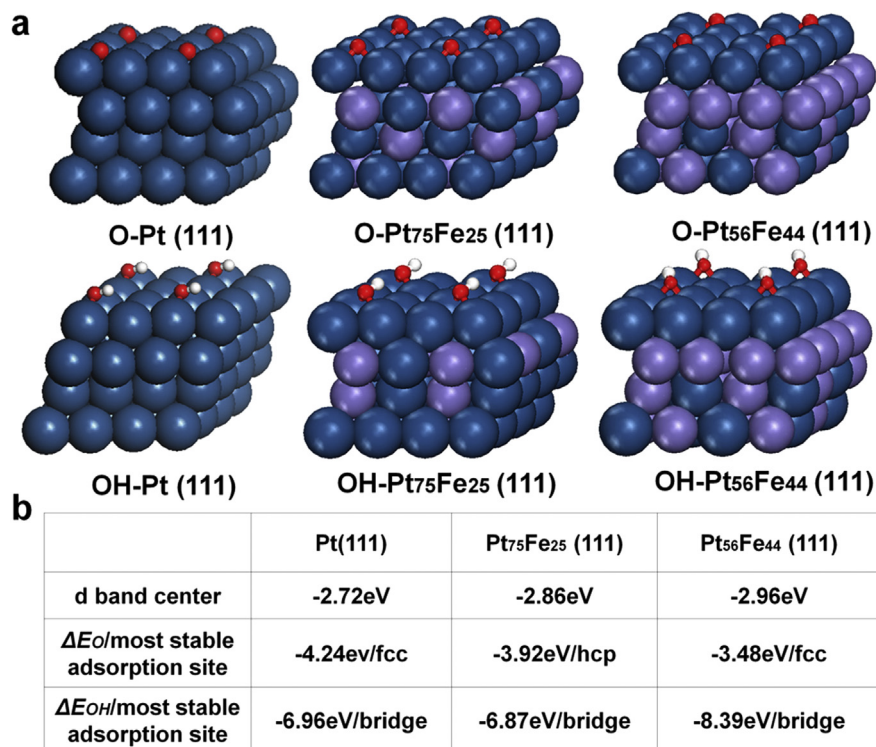

	Pt(111)	Pt$_{75}$Fe$_{25}$ (111)	Pt$_{56}$Fe$_{44}$ (111)
d band center	-2.72eV	-2.86eV	-2.96eV
ΔE_O/most stable adsorption site	-4.24ev/fcc	-3.92eV/hcp	-3.48eV/fcc
ΔE_{OH}/most stable adsorption site	-6.96eV/bridge	-6.87eV/bridge	-8.39eV/bridge

Fig. 7. (a) The most stable adsorbed schematic model of O and OH adsorbed on Pt(111), Pt$_{75}$Fe$_{25}$(111) and Pt$_{56}$Fe$_{44}$(111) slabs, (b) the d band center of Pt, ΔE_O, and ΔE_{OH} on Pt(111), Pt$_{75}$Fe$_{25}$(111) and Pt$_{56}$Fe$_{44}$(111) slabs.

architecture. NP–PtFe alloys hold great application potential as a promising cathode electrocatalyst for PEMFCs with the advantages of unique activity, high structure stability, low cost, and simple and high-yielding preparation without any assistance of organic solvent.

Acknowledgments

References

[1] A. Altamirano-Gutiérrez, A.M. Fernández, F.J. Rodríguez Varela, Int. J. Hydrogen Energy 38 (2013) 12657–12666.
[2] H.S. Chu, F. Tsau, Y.Y. Yan, K.L. Hsueh, F.L. Chen, J. Power Sources 176 (2008) 499–514.
[3] B. Erable, D. Féron, A. Bergel, ChemSusChem 5 (2012) 975–987.
[4] A. Ohma, S. Yamamoto, K. Shinihara, J. Power Sources 182 (2008) 39–47.
[5] Q.M. Wu, L.H. Jiang, L.T. Qi, L.Z. Yuan, E.D. Wang, G.G. Sun, Electrochim. Acta 123 (2014) 167–175.
[6] H.R. Colón-Mercado, B.N. Popov, J. Power Sources 155 (2006) 253–263.
[7] K. Jukk, J. Kozlova, P. Ritslaid, V. Sammelselg, N. Alexeyeva, K. Tammeveski, J. Electroanal. Chem. 708 (2013) 31–38.
[8] Q. Huang, H. Yang, Y. Tang, T. Lu, D.L. Akins, Electrochem. Commun. 8 (2006) 1220–1224.
[9] M. Zhiani, B. Rezaei, J. Jalili, Int. J. Hydrogen Energy 35 (2010) 9298–9305.
[10] C.H. Wang, H.C. Hsu, K.C. Wang, J. Colloid Interface Sci. 427 (2014) 91–97.
[11] X. Bo, J. Bai, B. Qi, L. Guo, Biosens. Bioelectron. 28 (2011) 77–83.
[12] M. Sevilla, C. Sanchís, T. Valdés-Solís, E. Morallón, A.B. Fuertes, Electrochim. Acta 54 (2009) 2234–2238.
[13] H.A. Gasteiger, N.M. Markovic, Science 324 (2009) 48–49.
[14] Y.N. Wu, S.H. Liao, H.F. Guo, X.Y. Hao, J. Power Sources 235 (2013) 135–141.
[15] C. Sealy, Mater. Today 11 (2008) 65–68.
[16] T.K. Lee, J.H. Jung, J.B. Kim, S.H. Hur, Int. J. Hydrogen Energy 37 (2012) 17992–18000.
[17] Z. Xu, H. Zhang, S.S. Liu, B.S. Zhang, H.X. Zhong, D.S. Su, Int. J. Hydrogen Energy 37 (2012) 17978–17983.
[18] Z. Xu, H. Zhang, H. Zhong, Q. Lu, Y. Wang, D. Su, Appl. Catal. B Environ. 111 (2012) 264–270.
[19] H.W. Liang, X. Cao, F. Zhou, C.H. Cui, W.J. Zhang, S.H. Yu, Adv. Mater. 23 (2011) 1467–1471.
[20] C.G. Chung, L. Kim, Y.W. Sung, J.W. Lee, J.S. Chung, Int. J. Hydrogen Energy 34 (2009) 8974–8981.
[21] J.G. Oh, W.H. Lee, H.S. Kim, Int. J. Hydrogen Energy 37 (2012) 2455–2461.
[22] T. Bligaard, J.K. Nørskov, Electrochim. Acta 52 (2007) 5512–5516.
[23] K. Shimizu, I.F. Cenga, C.M. Waia, Electrochem. Commun. 11 (2009) 691–694.
[24] T. Toda, H. Igarashi, M. Watanabe, J. Electroanal. Chem. 460 (1999) 258–262.
[25] A.R. Malheiro, J. Perez, H.M. Villullas, J. Power Sources 195 (2010) 3111–3118.
[26] J.H. Pikul, H.G. Zhang, J. Cho, P.V. Braun, W.P. King, Nat. Commun. 4 (2013) 1732.
[27] Z.H. Zhang, C. Zhang, J.Z. Sun, T.Y. Kou, Q.G. Bai, Y. Wang, Y. Ding, J. Mater. Chem. A 1 (2013) 3620–3628.
[28] Y. Ding, M.W. Chen, MRS Bull. 34 (2011) 569–576.
[29] J. Snyder, T. Fujita, M.W. Chen, J. Erlebacher, Nat. Mater. 9 (2010) 904–907.
[30] H.J. Qiu, J.L. Kang, P. Liu, A. Hirata, T. Fujita, M.W. Chen, J. Power Sources 247 (2014) 896–905.
[31] C.X. Xu, Y.Q. Liu, J.P. Wang, H.R. Geng, H.J. Qiu, J. Power Sources 199 (2012) 124–131.
[32] M. Oezaslan, P. Strasser, J. Power Sources 196 (2011) 5240–5249.
[33] J. Zhang, Y.W. Zhan, H.D. Bian, Z. Li, C.K. Tsang, C. Lee, H. Cheng, S.W. Shu, Y.Y. Li, J. Lu, J. Power Sources 257 (2014) 374–379.
[34] L. Liu, R. Scholz, E. Pippel, U. Gosele, J. Mater. Chem. 20 (2010) 5621–5627.
[35] C.X. Xu, Q. Li, Y.Q. Liu, J.P. Wang, H.R. Geng, Langmuir 28 (2012) 1886–1892.
[36] H. Zhao, L. Li, J. Yang, Y. Zhang, H. Li, Electrochem. Commun. 10 (2008) 876–879.
[37] J.B. Xu, K.F. Hua, G.Z. Sun, C. Wang, X.Y. Lv, Y.J. Wang, Electrochem. Commun. 8 (2006) 982–986.
[38] G. Kresse, J. Furthmüller, Phys. Rev. B 54 (1996) 11169–11186.
[39] J.P. Perdew, K. Burke, M. Ernzerhof, Phys. Rev. Lett. 77 (1996) 3865–3868.
[40] M. Methfessel, A.T. Paxton, Phys. Rev. B 40 (1989) 3616.
[41] T. Toda, H. Igarashi, H. Uchida, M. Watanabe, J. Electrochem. Soc. 146 (1999) 3750–3756.
[42] W. Yuan, K. Scott, H. Cheng, J. Power Sources 163 (2006) 323–329.
[43] R.Z. Yang, J. Leisch, P. Strasser, M.F. Toney, Chem. Mater. 22 (2010) 4712–4720.
[44] L.Y. Chen, H. Guo, T. Fujita, A. Hirata, W. Zhang, A. Inoue, M.W. Chen, Adv. Funct. Mater. 21 (2011) 4364–4370.
[45] H. Zhang, Q. Hao, H.R. Geng, C.X. Xu, Int. J. Hydrogen Energy 38 (2013) 10029–10038.
[46] W.W. Zhao, H. Zhang, M. Li, J. Inorg. Mater. (2013) 1217–1222.
[47] V.R. Stamenkovic, B. Fowler, B.S. Mun, G.F. Wang, P.N. Ross, C.A. Lucas, N.M. Markovic, Science 315 (2007) 493–497.
[48] B. Lim, M. Jiang, P.H.C. Camargo, E.C. Cho, J. Tao, X. Lu, Y. Zhu, Y. Xia, Science 324 (2009) 1302–1305.
[49] M. Leia, T.Z. Yang, W.J. Wang, K. Huang, R. Zhang, H.J. Yang, Y.G. Wang, W.H. Tang, Int. J. Hydrogen Energy 38 (2013) 205–211.
[50] M. Lei, C. Liang, Y.J. Wang, K. Huang, C.X. Ye, G. Liu, W.J. Wang, S.F. Jin, R. Zhang, D.Y. Fan, H.J. Yang, Y.G. Wang, Electrochim. Acta 113 (2013) 366–372.
[51] J. Prabhuram, T. Zhao, Z. Tang, R. Chen, Z. Liang, J. Phys. Chem. B 110 (2006) 5245–5252.
[52] A. Kabbabi, R. Faure, R. Durand, B. Beden, F. Hahn, J.M. Leger, C. Lamy, J. Electroanal. Chem. 444 (1998) 41–53.
[53] A.R. Malheiro, J. Perez, H.M. Villullas, J. Electrochem. Soc. 156 (2009) B51–B58.
[54] S. Zuluaga, S. Stolbov, J. Chem. Phys. 135 (2011) 134702.
[55] Y. Suo, L. Zhuang, J. Lu, Angew. Chem. Int. Ed. 46 (2007) 2862–2864.
[56] V. Stamenkovic, B.S. Mun, K.J.J. Mayrhofer, P.N. Ross, N.M. Markovic, J. Rossmeisl, J. Greeley, J.K. Norskov, Angew. Chem. Int. Ed. (2006) 2897–2901.
[57] H.L. Xin, S. Linic, J. Chem. Phys. 132 (2010) 221101.